Precessional dynamics of geometrically scaled magnetostatic spin waves in two-dimensional magnonic fractals

Jingyuan Zhou,[1,2,*] Mateusz Zelent,[3] Sergii Parchenko,[1,2] Zhaochu Luo,[1,2] Valerio Scagnoli,[1,2] Maciej Krawczyk,[3] Laura J. Heyderman,[1,2] and Susmita Saha[1,2,4,*]

[1]*Laboratory for Mesoscopic Systems, Department of Materials, ETH Zurich, 8093 Zurich, Switzerland*
[2]*Laboratory for Multiscale Materials Experiments, Paul Scherrer Institute, 5232 Villigen PSI, Switzerland*
[3]*Faculty of Physics, Adam Mickiewicz University, Poznan, Uniwersytetu Poznanskiego 2, Poznan PL-61-614, Poland*
[4]*Department of Physics, Ashoka University, 131029 Hariyana, India*

(Received 21 March 2022; revised 23 April 2022; accepted 25 April 2022; published 13 May 2022; corrected 18 July 2022)

The control of spin waves in periodic magnetic structures has facilitated the realization of many functional magnonic devices, such as band stop filters and magnonic transistors, where the geometry of the crystal structure plays an important role. Here, we report on the magnetostatic mode formation in an artificial magnetic structure, going beyond the crystal geometry to a fractal structure, where the mode formation is related to the geometric scaling of the fractal structure. Specifically, the precessional dynamics was measured in samples with structures going from simple geometric structures toward a Sierpinski carpet and a Sierpinski triangle. The experimentally observed evolution of the precessional motion could be linked to the progression in the geometric structures that results in a modification of the demagnetizing field. Furthermore, we have found sets of modes at the ferromagnetic resonance frequency that form a scaled spatial distribution following the geometric scaling. Based on this, we have determined the two conditions for such mode formation to occur. One condition is that the associated magnetic boundaries must scale accordingly, and the other condition is that the region where the mode occurs must not coincide with the regions for the edge modes. This established relationship between the fractal geometry and the mode formation in magnetic fractals provides guiding principles for their use in magnonics applications.

DOI: 10.1103/PhysRevB.105.174415

I. INTRODUCTION

In solid state physics, materials are often described in the context of crystals that consist of periodic arrays of atoms. However, there are many materials that do not belong to this category [1,2]. Some materials have ordered structures but do not possess translation symmetry, such as quasicrystal and fractal structures [1,3,4]. For example, for porous materials, the pores form a fractal structure and can be effectively described by the fractal theory [5,6]. Fractals, by definition, are composed of self-similar structures across different length scales, which look similar under different magnifications. This property is commonly referred to as dilation symmetry, which is the most distinctive feature of fractals [4]. There are many examples of fractals in nature, such as snowflakes, Romanesco broccoli, and coastlines. In addition, the geometry of fractals has been exploited in many artificial metamaterials for manipulating material properties [7–10]. For example, fractal cavities have been used to localize electromagnetic waves [7], and microwave fractal antennas can exhibit multiband behavior [8]. Additionally, many emergent phenomena in different physical systems exhibit fractal-like behaviors, such as the Hofstadter butterfly [11], and dynamic fractals generated from optical and spin-wave solitons [12–15].

The fractal geometry can also be implemented in magnetic systems to modify the magnetic properties, such as the hysteresis loop [16], the magnonic band structure, and the spin-wave localization. Various ferromagnetic structures with crystal geometries have been successfully exploited to engineer different spin-wave band structures [17–24], while the localization of spin waves and self-similarity in the spin-wave spectra have been observed in magnonic quasicrystals [25–29]. In a similar way, the fractal geometry should modify the corresponding spin-wave properties. Moreover, fractal structures possess a noninteger dimension, which is commonly referred to as the Hausdorff dimension or fractal dimension [30]. This dimension confines the magnetic interactions to between 1D and 2D, and hence fractals can modify the spin-wave dispersion in a unique way [31]. Early works on magnetic fractals were focused on diluted antiferromagnets, where the magnetic ions can form a percolating structure that is a statistical fractal [32]. Recently, the spin-wave spectra in square-based ferromagnetic Sierpinski carpet structures were also reported [33,34]. In Ref. [33], devil's staircase spin-wave spectra, remaining at all iteration steps in the exchange approximation, were theoretically predicted. The experimental realization of the square Sierpinski carpet up to the third iteration level with broadband ferromagnetic resonance measurements showed an increase of quantized spin-wave modes with the increase of the iteration level [34]. However, how the origin of the spin-wave modes depends

*jingyuan.zhou@psi.ch; susmita.saha@ashoka.edu.in

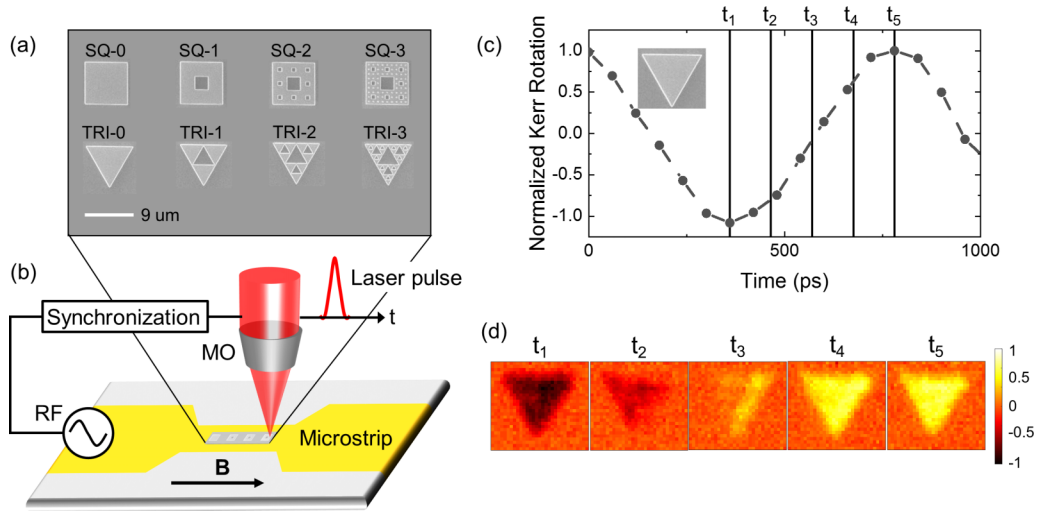

FIG. 1. (a) SEM image of the square (SQ) and triangular (TRI) structures. (b) Schematic of the TRSKM setup and the sample. (c), (d) TRSKM measurements of the sample TRI-0 at $B = 15$ mT and $f_{RF} = 3.7$ GHz. (c) Normalized time-resolved Kerr rotation. (d) Five normalized scanning Kerr rotation images, in the range $[-1, 1]$, measured from t_1 to t_5 at 360, 465, 570, 675, and 780 ps, respectively, which are indicated by the solid lines in (c).

on the scaling of the fractal geometry as well as experimental visualization of the spin-wave modes have not yet been reported.

In this paper, we demonstrate a method for analyzing the magnetostatic spin-wave modes in magnetic fractals with the increase of the iteration level of the fractal structure. We have observed a complex evolution of the spin-wave modes when a simple square is evolved toward a Sierpinski square whereas a single uniform spin-wave mode is observed when a simple triangle is developed toward a Sierpinski triangle [35]. By comparing the evaluation of spin-wave modes in the square structures when going from the first to third iteration, we confirmed experimentally the trend of the mode formation in magnetic fractals, which is directly related to the geometric scaling. To explain the experimental results, we have performed micromagnetic simulations, which show good agreement with the experimental observations. We found an important influence of the boundaries on the spin-wave spectra. In particular, if the magnetic boundaries are similar, the amplitude distribution of the spin-wave mode follows the geometric scaling to form scaled mode patterns in fractal-like structures with a change of the iteration level. Our observations point at the potential of 2D fractal structures to be implemented in novel types of functional magnonic devices.

II. EXPERIMENTAL DETAILS

A. Sample fabrication and design

Two sets of 20 nm thick $Ni_{83}Fe_{17}$ (Permalloy) samples with square and triangle shaped elements were fabricated on top of a microstrip transmission line using electron-beam (e-beam) lithography combined with DC magnetron sputtering with a base pressure of $\sim 3 \times 10^{-8}$ mbar, followed by a liftoff process. To prevent oxidation, a 2-nm Al layer was deposited on top of the ferromagnetic layer. The transmission line was fabricated on top of a high-resistivity Si substrate, using e-beam lithography in conjunction with e-beam evaporation, followed by a liftoff process. The composition of the transmission line is Cr(2 nm)/Cu(100 nm)/Cr(2 nm), and its width is 20 μm.

For square structures [see Fig. 1(a)], the simplest is SQ-0, a featureless square whose side length is 9 μm. To generate the next structure SQ-1, a 3 μm $\times$ 3 μm square is removed at the center of SQ-0. SQ-1 is defined as the base structure with iteration number 1. This base structure can be considered to be made up of eight similar squares, each with a side length 1/3 of SQ-0. For the next structure, SQ-1 is scaled by a factor of 1/3, and repeated 8 times following the pattern of SQ-1 to generate SQ-2, with iteration number 2. Following this iteration, SQ-3 is generated based on SQ-2 and has an iteration number 3. This iteration process can in principle be continued to go to infinity to create an ideal fractal, which is commonly referred to as a Sierpinski carpet. However, experimentally this is limited by the smallest feature size that can be created with electron beam lithography.

For triangular samples [see Fig. 1(a)], TRI-0 is an equilateral triangle with the side length of 10 μm. To generate TRI-1, an equilateral triangle is removed, whose vertices are at the centers of the three sides of TRI-0. Similar to the square samples, TRI-1 is defined as the base structure for the triangular sample set, and TRI-1 can also be considered as three triangles with a side length of 5 μm. To further generate TRI-2 and TRI-3, a similar iteration process to that used for the square fractals can be used, but with a scaling factor of 1/2. The details are given in the Supplemental Material [36].

B. Time-resolved precessional dynamics

To characterize the precessional dynamics, a time-resolved scanning Kerr microscope (TRSKM) setup was employed to obtain both time and spatially resolved images with magnetic contrast, taking advantage of the magneto-optical Kerr effect (MOKE) [37,38], as shown in Fig. 1(b). It is based on an electrical excitation and optical detection

pump-probe setup with an ultrafast fiber laser system having a central wavelength of 1030 nm, pulse width of ∼50 fs, and repetition rate of 200 kHz [37,38]. The laser beam is guided through a variable delay stage, and subsequently focused on to the sample using a long working distance microscope objective with numerical aperture of 0.55 to probe the precessional dynamics using the polar MOKE geometry. As shown in Fig. 1(b), a radio-frequency (RF) signal from the synthesizer (ADF5355, Analog Devices), which is synchronized with the laser pulse, is passed through the microstrip transmission line to generate the RF magnetic field for excitation of the precession of the magnetization in the magnetic structures. To retrieve the signal, a lock-in detection scheme is used (HF2, Zurich Instruments), where the ∼2 kHz reference signal from the lock-in amplifier is used to drive an RF switch to modulate the RF current.

For each sample, the time-resolved precession was measured in the frequency range $f_{RF} = 2.0$–5.5 GHz, with a step size of 0.1 GHz. For these measurements, the laser beam was slightly defocused in order to fully cover the geometric structures. The precessional amplitude for each excitation frequency was subsequently extracted in order to obtain a complete frequency spectrum. Next, the peaks in the frequency spectra were chosen at which the 2D scanning Kerr images were measured. For these measurements, the laser beam was completely focused to the spot size ∼1.1 μm. For all the scanning Kerr images, the samples were scanned in steps of 400 nm, and measurements were taken at a specific time instant where the corresponding phase value of the sinusoidal oscillation was $\pi/2$. For example, for TRI-0 at 3.7 GHz, the delay stage was moved to t_5 [see Fig. 1(c)]. It should be noted that this time value is different for different frequencies.

An external magnetic field that is sufficient to saturate the samples (15 mT) is applied parallel to the transmission line (see the hysteresis loops in the Supplemental Material [39]), which provides the RF signal to excite spin waves. Subsequently, the spatial distribution of the out-of-plane component of the magnetization m_z at different times is acquired using the TRSKM technique as shown in Figs. 1(c) and 1(d).

III. RESULTS AND DISCUSSION

A. Precessional dynamics of the samples

First looking at the precessional dynamics observed for the triangular samples, as shown in Fig. 2, we find that there is one mode for each sample, indicated by the red marker, where a uniform distribution of m_z in each triangle is present. For TRI-0, two modes at 3.2 GHz and 3.7 GHz are observed whereas for TRI-1 and TRI-2, only a single mode at 3.7 GHz is present. It is observed from the scanning Kerr images [see Fig. 2(c)] that the modes are quite uniformly distributed throughout the triangular structures. The observed dynamics is isolated in the individual subtriangles since each triangular substructure has only point contacts with its neighbors at the vertices. However, the same frequencies on the last two iteration levels point at in-phase oscillations in all triangles, and lack of the structural effects above the TRI-1 level for

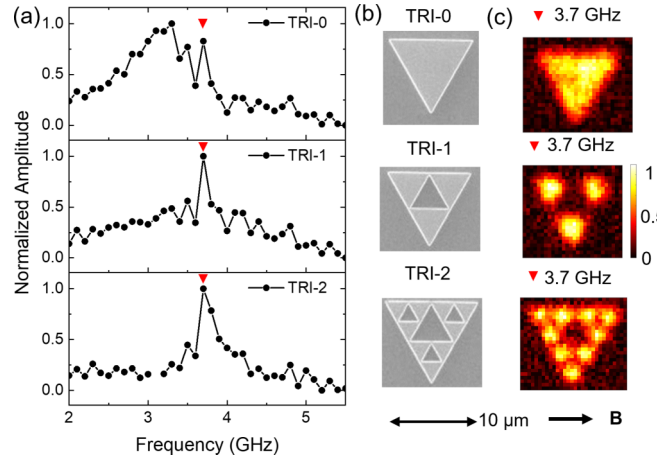

FIG. 2. TRSKM measurements of triangular structures. (a) Frequency spectra of the triangular structures TRI-0 to TRI-2. (b) SEM images of structures TRI-0 to TRI-2, with the magnetic field direction indicated next to TRI-2. (c) Normalized scanning Kerr images measured for the three samples. The mode is indicated by red markers in (a).

this detected mode. For TRI-3, the scanning Kerr image is not well resolved due to the limited spatial resolution (see the Supplemental Material [40]), and hence no conclusions can be obtained.

For square samples, the precessional dynamics becomes more complex when going from SQ-0 to SQ-2, in terms of both the frequency spectra [see Fig. 3(a)] and scanning Kerr images [see Fig. 3(c)]. For SQ-0, a broad peak is observed in the frequency spectrum. For the corresponding scanning Kerr image at 3.7 GHz, it can be seen that m_z is uniformly distributed across the whole square. For SQ-1, the frequency peak has a small redshift, compared with that of SQ-0 and, for the mode at 3.1 GHz, the m_z distribution is more concentrated at the upper and lower parts of SQ-1. Moving to SQ-2, the dynamics becomes complex. In the frequency spectrum, multiple peaks are present, which are indicated by the three different colored markers in Fig. 3(a). For a better description, several geometric substructures are defined for SQ-2, as shown in Fig. 3(b). L1–L4 are the four edges with width of 9 μm, s1 is the central 3 μm × 3 μm square hole, and s2 corresponds to the eight 1 μm × 1 μm square holes. For the mode at 3.4 GHz, the distribution of m_z in the scanning Kerr image is concentrated along the peripheries of the eight s2 voids. When the frequency is increased to 3.7 GHz, it can be seen that the higher intensity parts of the m_z distribution form several patches next to the s2 voids. When the excitation frequency is further increased to 4.4 GHz, the patches start to merge together, forming four slightly curved wormlike structures that are oriented at 45° and 135° with respect to the applied field. Moving to SQ-3, the dynamics should be in principle more complex than SQ-2, since it has 64 smaller square voids with width ∼333 nm. However, since the size of the smallest structures is below the size of the laser spot, 1.1 μm, the spatial distribution of the dynamics becomes difficult to resolve (see the Supplemental Material [40]).

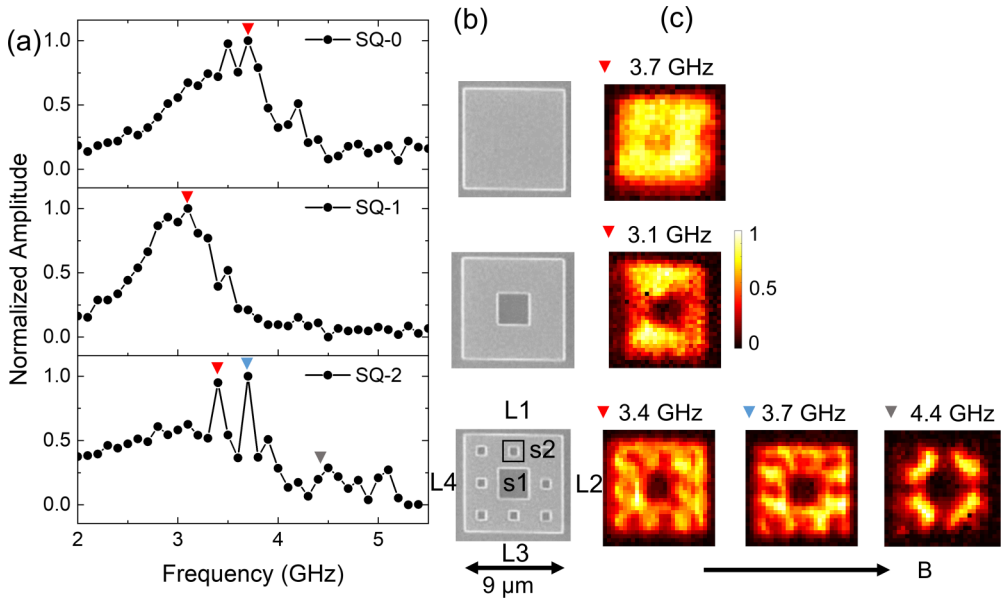

FIG. 3. TRSKM measurements of square structures. (a) Frequency spectra of square structures SQ-0 to SQ-2. (b) SEM images of structures SQ-0 to SQ-2. For SQ-2, L1–L4 are the four edges with width of 9 μm, s1 is the central 3 μm × 3 μm square hole, and s2 corresponds to the eight 1 μm × 1 μm square holes. (c) Normalized scanning Kerr images of the different modes for the three structures. The modes corresponding to different frequencies are indicated by different colored markers in (a).

B. Mode analysis for SQ-2

To understand the dynamics, micromagnetic simulations based on the Landau-Lifshitz-Gilbert (LLG) equation were performed using MuMax3 [41]. The parameters used in the simulations were damping $\alpha = 0.02$, exchange constant 1.3×10^{-12} J/m, magnetocrystalline anisotropy constant $K = 0$, saturation magnetization $\mu_0 M_S = 0.956$ T, and cell size $2 \times 2 \times 20$ nm^3. To match the experimentally observed scanning Kerr images, a single-frequency excitation of the form $A\sin(2\pi ft)$ is used, where f and A are the excitation frequency and amplitude. To simulate broad band spin wave frequency spectra, another set of micromagnetic simulations are performed, using an external microwave magnetic field of the form $A\,\mathrm{sinc}(2\pi f_{\mathrm{cut}}t) = A\sin(2\pi ft)/(2\pi f_{\mathrm{cut}}t)$ where A is 5.0×10^{-5} T and f_{cut} (cutoff frequency) is 15 GHz.

For the triangular structure, the micromagnetic simulations confirm the presence of a single mode and the mode-profile calculation also demonstrates the discrete dynamics of the individual subtriangles shown in the Supplemental Material [42]. The spin-wave dynamics for the triangular structure is relatively simple compared to the complex dynamics observed in the square structure. Therefore, extended micromagnetic simulations are performed for the square structure to obtain an in-depth understanding of the complex dynamics.

For the square structure, initially the system is excited using a single-frequency sinusoidal excitation with two simulation frequencies of 3.66 and 4.56 GHz, which are close to the experimental values as shown in Fig. 4. For both frequencies, in order to be consistent with the experimental conditions, the snapshots of the simulated spatial distributions of m_z are taken at the two times indicated by the red dashed lines in Fig. 4(a), which correspond to the phase value close to $\pi/2$ for each sinusoidal oscillation. In Fig. 4(b), it can be seen that, for 3.66 GHz, there are eight lobelike structures located in between the s2 structures and, for 4.56 GHz, there are four wormlike structures at the corners of the s1 structure, demonstrating good agreement with the experimental results in Fig. 4(c) for SQ-2. The small discrepancies between the experimental and simulation frequency and phase values may be due to a variety of effects, such as edge roughness and a possible difference in the saturation magnetization values.

The simulated frequency spectrum, excited using a sinc function to give a complete overview of the precessional dynamics for SQ-2, is shown in Fig. 5(a). As indicated by the different color shaded areas, the observed modes are classified into three categories, namely the edge mode (E), the first-order localized mode (M), and the higher-order mode (HO). The complete mode profiles with amplitude and phase distributions are shown in the Supplemental Material [43]. Here, we focus on the three first-order localized modes, M1, M2, and M3, with frequency values of 3.66, 4.18, and 5.08 GHz, respectively, as shown in Fig. 5(b). For M1, the mode forms four vertically orientated lobelike structures, each located in between the two vertical edges of s2. For M2, the mode forms four rounded structures, each located in between the two horizontal edges of s2. For M3, the mode forms a rather different pattern, which contains eight barlike structures, four in the upper part, and four in the lower part of SQ-2. Since the amplitudes of these three modes are concentrated at locations near the s2 structures and each local precession is almost uniform with a phase variation smaller than 0.07π (see the Supplemental Material [43]), we refer to these three modes as the first-order localized modes.

To ascertain the origin of these modes, the total internal field distribution B_{tot} for the static magnetic system is calculated, which consists of three contributions: the applied magnetic field, the demagnetizing field, and the exchange field. As shown in Fig. 5(c), it can be seen that the modes M1 to M3 appear at the regions with $B_{\mathrm{tot}} \sim 15$ mT, which is the value of the applied magnetic field. In these regions, the total

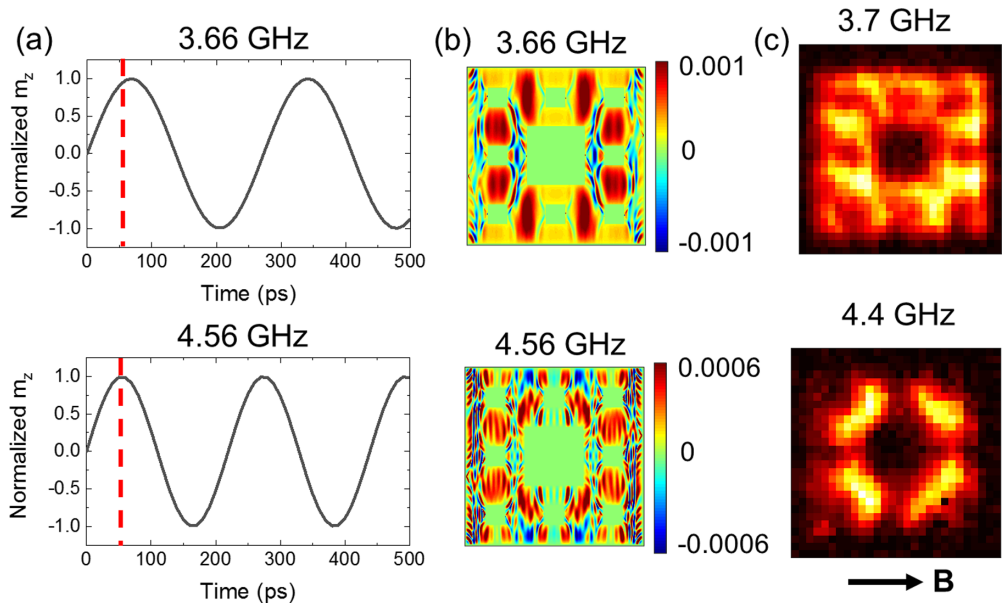

FIG. 4. Comparison between the simulated and experimental results for SQ-2. (a) Simulated time-resolved precession using two single-frequency excitations at 3.66 and 4.56 GHz. (b) Simulated m_z distributions that are taken at the time indicated by the red dashed lines in (a). The color maps are set to optimize the image contrast for the spatial distribution. (c) Experimental scanning Kerr images at the phase value of $\pi/2$ for the corresponding sinusoidal oscillation at frequencies of 3.7 and 4.4 GHz. The color scale for (c) is similar to that used in Fig. 3(c).

internal field is dominated by the applied magnetic field. As a result, the local precessional dynamics is similar to the ferromagnetic resonance of a thin film. However, due to structuring and the local demagnetizing field, the uniform precession becomes confined and splits into different frequencies. To quantify the influence of the locally varying demagnetizing field, five line profiles of B_{tot} at five different regions are taken, as indicated by the dotted lines in Fig. 5(c). According to the

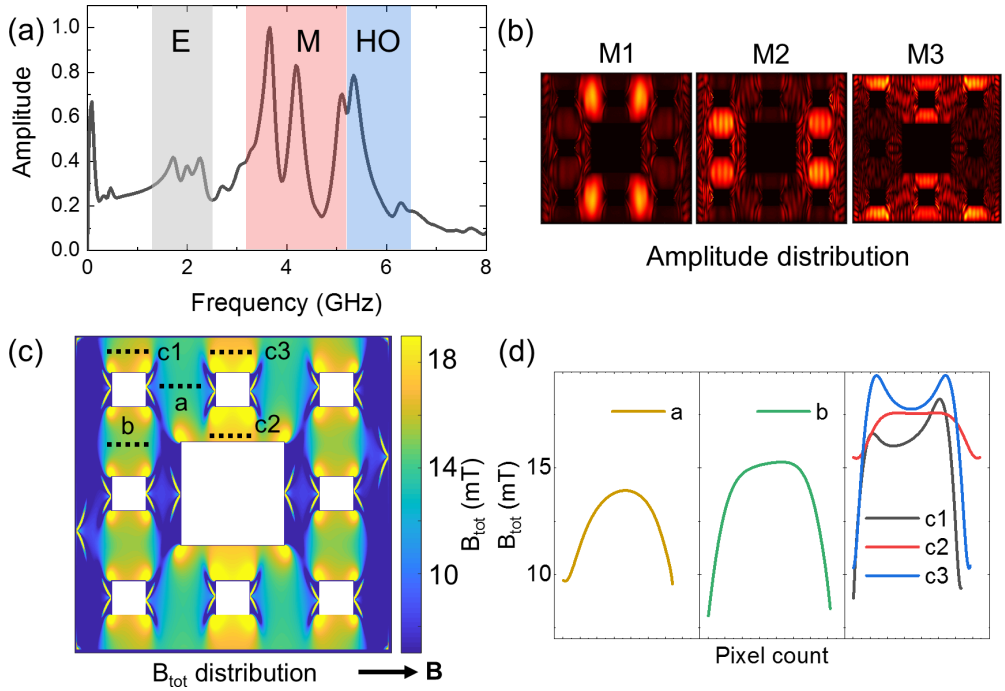

FIG. 5. Analysis of simulated modes for SQ-2. (a) Frequency spectrum of SQ-2 at 15 mT, with the edge modes (E), the first-order localized modes (M), and the higher-order modes (HO) indicated with different color shaded areas. (b) Amplitude distributions of the three modes M1 (3.66 GHz), M2 (4.18 GHz) and M3 (5.08 GHz). (c) Total field distribution B_{tot} within the magnetic structure of SQ-2. The external magnetic field is applied along the horizontal direction, as indicated by the arrow. (d) Five line profiles of the total field distribution along the horizontal direction, with positions indicated by dashed lines in (c).

average B_{tot} value at the plateaus [see Fig. 5(d)], the fives regions are classified into three groups a, b, and c1–c3. For the line profiles at c1–c3, the B_{tot} values are within the same range 16–19 mT, and hence they are ascribed to the same group. It can be seen that the relationship of the B_{tot} value at these regions is

$$B_{\text{tot}}^{\text{c1,c2,c3}} > B_{\text{tot}}^{\text{b}} > B_{\text{tot}}^{\text{a}}. \tag{1}$$

This relationship is in exact agreement with the frequency relationship of the three modes M1 to M3, which is

$$f_{\text{M3}} > f_{\text{M2}} > f_{\text{M1}}. \tag{2}$$

The agreement between the two relationships again confirms the first-order localized nature of the three modes, and provides a semiquantitative explanation for their frequency relationship.

Having analyzed the three modes for SQ-2, we look back at the experimental observations shown in Fig. 4(c). Now, the experimentally observed three modes should be ascribed to the category of the first-order localized mode. It is difficult to predict which mode (M1 or M2) corresponds to the experimentally observed mode at 3.7 GHz and 4.4 GHz. It seems to be a combination of M1 and M2 (see the Supplemental Material [44]).

C. Mode formation in magnetic fractals

To reveal the role of the fractal geometry, we performed micromagnetic simulations for SQ-3, again using a sinc excitation similar to that used for SQ-2. From the simulated results, the three first-order localized modes at 4.30 (M1′), 6.04, and 7.55 (M3′) GHz are selected, whose amplitude and phase distribution are shown in Fig. 6(a) and the Supplemental Material [45], respectively. First, we note that there is a scaling relation between samples SQ-3 and SQ-2; namely, SQ-3 is composed of eight scaled SQ-2(j) substructures with a scaling factor of 1/3 [see Fig. 6(d)]. Next, we compare the modes shown in Figs. 6(a) and 6(b). It can be observed that M1 and M1′, and M3 and M3′, have some geometric similarities in the amplitude distribution. In particular, as shown in Fig. 6(a), the amplitude distributions of M1′ and M3′ within the two substructures SQ-2(2) and SQ-2(6) are exactly two scaled patterns of the amplitude distributions of M1 and M3, respectively. For the other six scaled SQ-2(j) substructures, they either exhibit part of the scaled patterns from M1 and M3, or exhibit no modes. From these observations, we infer that M1 and M3 evolve into M1′ and M3′, respectively, and exhibit scaled amplitude distributions in the corresponding scaled SQ-2(j) substructures but with certain modifications. In contrast, for the mode at 6.04 GHz, the amplitude distribution is not located within the eight scaled substructures SQ-2(j), but at the center locations where SQ-2(4) and SQ-2(8) connect with their neighboring substructures.

In order to explain the observed formation of the different modes, we need to find the necessary conditions for a scaled mode pattern to occur in the scaled SQ-2(j) substructures of SQ-3. As shown in Fig. 6(b), the formation of modes M1 to M3 is associated with different geometric edges L1–L4 in the SQ-2 structure (see Fig. 6(d) and the Supplemental Material [46] for the definition of the edges). When SQ-2 is scaled into the SQ-2(j) substructures in SQ-3, some edges of the square substructures associated with L1 to L4 disappear, and the other edges are scaled accordingly. Therefore, we identify the contributions from the edges to these three modes, which are L1 and L3 edges for both M1 and M3, and L2 and L4 for M2. Accordingly, we can explain the evolution of M1 to M1′, because for SQ-2(2) and SQ-2(6), both L1 and L3 are present, and hence two scaled patterns of M1 are observed. Such observations lead to the first necessary condition for a scaled mode pattern to occur, which is the presence of the associated structural edges from the SQ-2 structure within the SQ-2(j) substructure.

We can carry out a similar analysis of the evolution of M3 to M3′ by considering the L1 and L3 edges. However, here a difference can be also seen; namely, a part of the scaled patterns is missing at the regions indicated by the white boxes in Fig. 6(a). To understand this difference, it should be noted that these regions correspond to those where the edge modes

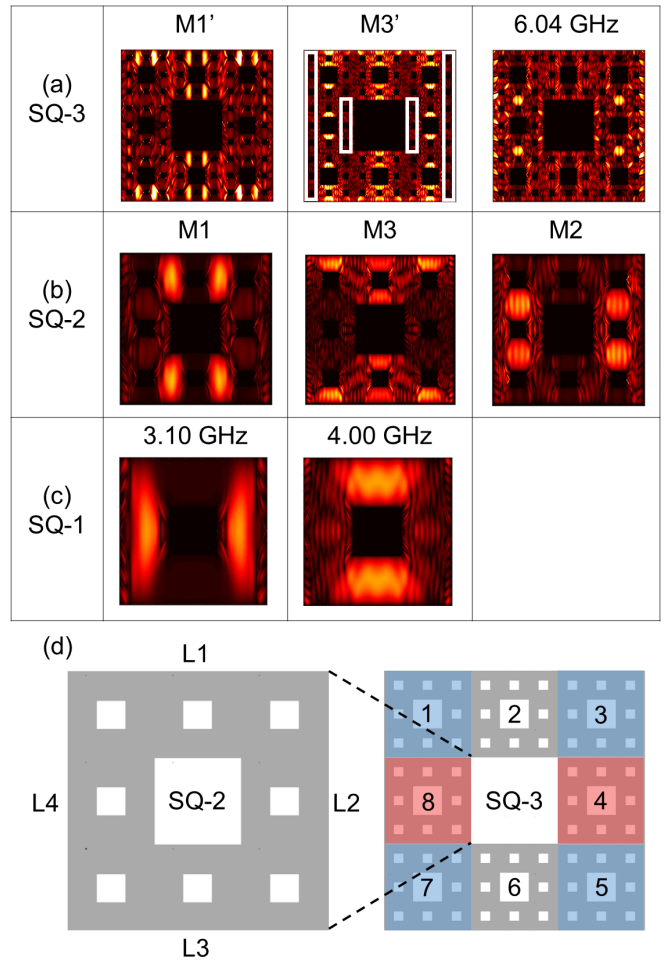

FIG. 6. Simulated mode evolution from SQ-1 to SQ-3. (a) Amplitude distributions of the three modes for SQ-3 at 4.30 GHz (M1′), 7.55 GHz (M3′), and 6.04 GHz. The white boxes indicate the regions where the edge modes occur. (b) Amplitude distributions of the three modes M1 to M3 for SQ-2. (c) Amplitude distributions of the two modes at 3.10 and 4.00 GHz for SQ-1. (d) Schematics of structures SQ-2 and SQ-3, with different color shaded areas indicating the eight scaled SQ-2 structures SQ-2(j), $j = 1$–8.

occur. Therefore, at 7.55 GHz (the frequency of M3′), no first-order modes can be observed in these regions. Thus, we find the second condition for a scaling of the modes, which is to exclude the regions of the edge mode localizations. After evaluating these two conditions for M2, it can be seen that none of the SQ-2(j) substructures can fulfill the two conditions simultaneously. Therefore, M2 cannot evolve to a mode in SQ-3 with a self-similar amplitude distribution.

To further confirm our findings, we examine the mode evolution from SQ-1 to SQ-2, as shown in Figs. 6(b) and 6(c). Similarly, SQ-2 can be viewed as 8 scaled SQ-1(j) substructures. In this way, it can be seen that the mode at 4.00 GHz evolves into M3 in a similar fashion to the evolution of M1 into M1′, with the associated magnetic boundaries being L1 and L3. Therefore, the mode M3′ can actually be traced back to the mode at 4.00 GHz in SQ-1. In contrast, the mode at 3.10 GHz in SQ-1 does not evolve into a mode in SQ-2 in the same way that M2 does not evolve into a mode in SQ-3.

Finally, we extend our argument to the most general case, i.e., the mode evolution from SQ-i to SQ-($i+1$), where i is the iteration number. We can infer that, for any fractal-like structure with iteration number $i+1$, the mode profiles can be analyzed using the mode profiles of the structure with iteration number i. Our argument is valid as long as the dominating interaction in these structures is magnetostatic since, following Maxwell's equations, the distribution of the magnetostatic field can remain geometrically self-similar after scaling, if all the boundary conditions are scaled accordingly. These findings provide a new perspective for analyzing the magnetostatic modes in fractal-like structures, which is effectively a "reversal" of the iteration process of the fractal generation. This perspective can be extremely important when analyzing a fractal structure with a large iteration number, since it is now possible to reduce the complexity of the analysis by considering the mode profiles from the structure with a lower iteration.

IV. CONCLUSION

To conclude, we have determined the evolution of the magnetostatic spin-wave modes from a simple geometric structure toward a Sierpinski carpet and Sierpinski triangle by imaging the precessional dynamics using TRSKM. In particular, we have measured the frequency spectra of spin-wave oscillations excited by the RF magnetic field and also imaged the m_z distribution at a particular time for the different spin-wave modes. To the best of our knowledge, the imaging of spin waves in magnetic fractals, namely the Sierpinski square and triangle, has not been explored yet. In general, we find a simple evolution for the Sierpinski triangle from TRI-0 to TRI-2 whereas the observed dynamics in the Sierpinski square from SQ-0 to SQ-2 evolves from a single-frequency spectrum into a multiple-frequency spectrum with different spatial distributions. To obtain the complete mode profiles and explain the experimental results, further micromagnetic simulations were performed for SQ-2 and SQ-3. For SQ-2, the precessional dynamics is analyzed in the context of the total field distribution. Using this method, the formation of the three different types of modes in SQ-2, as well as the frequency relationship for the three first-order localized modes, is explained. For SQ-3, the simulated dynamics is found to be related to the modes in SQ-2 via the scaling relation. We find that the amplitude distribution of the magnetostatic mode follows the geometric scaling to form scaled mode patterns in fractal-like structures with one more iteration. However, for this to occur, we need to consider the associated magnetic boundaries and to exclude the regions where the edge modes exist. Finally, we provided a method to predict the distribution of the spin wave modes within the fractal structure by only considering their magnetic boundaries. In contrast to the precessional dynamics in magnonic crystals where the dynamics is dominated by the eigenmodes in the unit cell due to translation symmetry [17,18,20–24], magnetic fractals exhibit a more complex amplitude distribution that is defined by the geometric scaling and resembles all the features of the geometric structures on different length scales. Such complex dynamics inherits the geometric hierarchy of the fractal structures, and can be exploited to build functional magnonic systems that require a hierarchical architecture.

The data that support this study are available via the Zenodo repository [47].

ACKNOWLEDGMENTS

This project is funded by the Swiss National Science Foundation (Project No. 200020_172774). J.Z. acknowledges fruitful discussions with Dr. Peter Derlet and Dr. Aleš Hrabec. S.S. acknowledges support from an ETH Zurich postdoctoral fellowship and the Marie Curie Actions for People COFUND program. M.K. and M.Z. acknowledge financial support from the National Science Center Poland with Project No. UMO-2020/37/B/ST3/03936. Simulations were partially performed at the Poznan Supercomputing and Networking Center (Grant No. 398).

[1] D. Shechtman, I. Blech, D. Gratias, and J. W. Cahn, Metallic Phase with Long-Range Orientational Order and No Translational Symmetry, Phys. Rev. Lett. **53**, 1951 (1984).

[2] L. Berthier and G. Biroli, Theoretical perspective on the glass transition and amorphous materials, Rev. Mod. Phys. **83**, 587 (2011).

[3] J. Feder, *Fractals* (Springer Science & Business Media, 2013).

[4] T. Nakayama and K. Yakubo, *Fractal Concepts in Condensed Matter Physics* (Springer Science & Business Media, 2003).

[5] X. Shen, L. Li, W. Cui, and Y. Feng, Improvement of fractal model for porosity and permeability in porous materials, Int. J. Heat Mass Transf. **121**, 1307 (2018).

[6] Q. Zeng, M. Luo, X. Pang, L. Li, and K. Li, Surface fractal dimension: An indicator to characterize the microstructure of cement-based porous materials, Appl. Surf. Sci. **282**, 302 (2013).

[7] M. W. Takeda, S. Kirihara, Y. Miyamoto, K. Sakoda, and K. Honda, Localization of Electromagnetic Waves in

Three-Dimensional Fractal Cavities, Phys. Rev. Lett. **92**, 093902 (2004).

[8] C. Puente-Baliarda, J. Romeu, R. Pous, and A. Cardama, On the behavior of the Sierpinski multiband fractal antenna, IEEE Trans. Antennas Propag. **46**, 517 (1998).

[9] S. N. Kempkes, M. R. Slot, S. E. Freeney, S. J. Zevenhuizen, D. Vanmaekelbergh, I. Swart, and C. M. Smith, Design and characterization of electrons in a fractal geometry, Nat. Phys. **15**, 127 (2019).

[10] S. Sederberg and A. Elezzabi, Sierpiński fractal plasmonic antenna: A fractal abstraction of the plasmonic bowtie antenna, Opt. Express **19**, 10456 (2011).

[11] D. R. Hofstadter, Energy levels and wave functions of Bloch electrons in rational and irrational magnetic fields, Phys. Rev. B **14**, 2239 (1976).

[12] M. Soljacic, M. Segev, and C. R. Menyuk, Self-similarity and fractals in soliton-supporting systems, Phys. Rev. E **61**, R1048 (2000).

[13] S. Sears, M. Soljacic, M. Segev, D. Krylov, and K. Bergman, Cantor Set Fractals from Solitons, Phys. Rev. Lett. **84**, 1902 (2000).

[14] M. Segev, M. Soljačić, and J. M. Dudley, Fractal optics and beyond, Nat. Photonics **6**, 209 (2012).

[15] M. Wu, B. A. Kalinikos, L. D. Carr, and C. E. Patton, Observation of Spin-Wave Soliton Fractals in Magnetic Film Active Feedback Rings, Phys. Rev. Lett. **96**, 187202 (2006).

[16] K. Szulc, F. Lisiecki, A. Makarov, M. Zelent, P. Kuświk, H. Głowiński, J. W. Kłos, M. Münzenberg, R. Gieniusz, J. Dubowik, F. Stobiecki, and M. Krawczyk, Remagnetization in arrays of ferromagnetic nanostripes with periodic and quasiperiodic order, Phys. Rev. B **99**, 064412 (2019).

[17] M. Krawczyk and D. Grundler, Review and prospects of magnonic crystals and devices with reprogrammable band structure, J. Phys.: Condens. Matter **26**, 123202 (2014).

[18] T. Sebastian, Y. Ohdaira, T. Kubota, P. Pirro, T. Brächer, K. Vogt, A. Serga, H. Naganuma, M. Oogane, Y. Ando *et al.*, Low-damping spin-wave propagation in a micro-structured $Co_2Mn_{0.6}Fe_{0.4}Si$ Heusler waveguide, Appl. Phys. Lett. **100**, 112402 (2012).

[19] A. Conca, J. Greser, T. Sebastian, S. Klingler, B. Obry, B. Leven, and B. Hillebrands, Low spin-wave damping in amorphous $Co_{40}Fe_{40}B_{20}$ thin films, J. Appl. Phys. **113**, 213909 (2013).

[20] S. Saha, R. Mandal, S. Barman, D. Kumar, B. Rana, Y. Fukuma, S. Sugimoto, Y. Otani, and A. Barman, Tunable magnonic spectra in two-dimensional magnonic crystals with variable lattice symmetry, Adv. Funct. Mater. **23**, 2378 (2013).

[21] Z. Wang, V. Zhang, H. Lim, S. Ng, M. Kuok, S. Jain, and A. Adeyeye, Observation of frequency band gaps in a one-dimensional nanostructured magnonic crystal, Appl. Phys. Lett. **94**, 083112 (2009).

[22] Z. K. Wang, V. L. Zhang, H. S. Lim, S. C. Ng, M. H. Kuok, S. Jain, and A. O. Adeyeye, Nanostructured magnonic crystals with size-tunable bandgaps, ACS Nano **4**, 643 (2010).

[23] S. Tacchi, F. Montoncello, M. Madami, G. Gubbiotti, G. Carlotti, L. Giovannini, R. Zivieri, F. Nizzoli, S. Jain, A. Adeyeye *et al.*, Band Diagram of Spin Waves in a Two-Dimensional Magnonic Crystal, Phys. Rev. Lett. **107**, 127204 (2011).

[24] S. Saha, J. Zhou, K. Hofhuis, A. Kákay, V. Scagnoli, L. J. Heyderman, and S. Gliga, Spin-wave dynamics and symmetry breaking in an artificial spin ice, Nano Lett. **21**, 2382 (2021).

[25] F. Lisiecki, J. Rychły, P. Kuświk, H. Głowiński, J. W. Kłos, F. Groß, N. Träger, I. Bykova, M. Weigand, M. Zelent *et al.*, Magnons in a Quasicrystal: Propagation, Extinction, and Localization of Spin Waves in Fibonacci Structures, Phys. Rev. Appl. **11**, 054061 (2019).

[26] F. Lisiecki, J. Rychły, P. Kuświk, H. Głowiński, J. W. Kłos, F. Groß, I. Bykova, M. Weigand, M. Zelent, E. J. Goering, G. Schütz, G. Gubbiotti, M. Krawczyk, F. Stobiecki, J. Dubowik, and J. Gräfe, Reprogrammability and Scalability of Magnonic Fibonacci Quasicrystals, Phys. Rev. Appl. **11**, 054003 (2019).

[27] V. S. Bhat and D. Grundler, Angle-dependent magnetization dynamics with mirror-symmetric excitations in artificial quasicrystalline nanomagnet lattices, Phys. Rev. B **98**, 174408 (2018).

[28] S. Watanabe, V. S. Bhat, K. Baumgaertl, and D. Grundler, Direct observation of worm-like nanochannels and emergent magnon motifs in artificial ferromagnetic quasicrystals, Adv. Funct. Mater. **30**, 2001388 (2020).

[29] S. Watanabe, V. S. Bhat, K. Baumgaertl, M. Hamdi, and D. Grundler, Direct observation of multiband transport in magnonic Penrose quasicrystals via broadband and phase-resolved spectroscopy, Sci. Adv. **7**, eabg3771 (2021).

[30] C. McMullen, The Hausdorff dimension of general Sierpiński carpets, Nagoya Math. J. **96**, 1 (1984).

[31] J. Rychły, J. W. Kłos, M. Mruczkiewicz, and M. Krawczyk, Spin waves in one-dimensional bicomponent magnonic quasicrystals, Phys. Rev. B **92**, 054414 (2015).

[32] U. Nowak and K.-D. Usadel, Diluted antiferromagnets in a magnetic field: A fractal-domain state with spin-glass behavior, Phys. Rev. B **44**, 7426 (1991).

[33] P. Monceau and J.-C. S. Lévy, Spin waves in deterministic fractals, Phys. Lett. A **374**, 1872 (2010).

[34] C. Swoboda, M. Martens, and G. Meier, Control of spin-wave excitations in deterministic fractals, Phys. Rev. B **91**, 064416 (2015).

[35] K. J. Falconer and B. Lammering, Fractal properties of generalized Sierpiński triangles, Fractals **6**, 31 (1998).

[36] See Supplemental Material Fig. S1 at http://link.aps.org/supplemental/10.1103/PhysRevB.105.174415 for SEM images of the triangular structures with different iteration numbers.

[37] J. Zhou, S. Saha, Z. Luo, E. Kirk, V. Scagnoli, and L. J. Heyderman, Ultrafast laser induced precessional dynamics in antiferromagnetically coupled ferromagnetic thin films, Phys. Rev. B **101**, 214434 (2020).

[38] S. Saha, P. Flauger, C. Abert, A. Hrabec, Z. Luo, J. Zhou, V. Scagnoli, D. Suess, and L. J. Heyderman, Control of damping in perpendicularly magnetized thin films using spin-orbit torques, Phys. Rev. B **101**, 224401 (2020).

[39] See Supplemental Material Fig. S2 at http://link.aps.org/supplemental/10.1103/PhysRevB.105.174415 for hysteresis loops for the square and triangular structures.

[40] See Supplemental Material Fig. S3 at http://link.aps.org/supplemental/10.1103/PhysRevB.105.174415 for time-resolved scanning Kerr microscopy measurements of structures SQ-3 and TRI-3.

[41] A. Vansteenkiste, J. Leliaert, M. Dvornik, M. Helsen, F. Garcia-Sanchez, and B. Van Waeyenberge, The design

and verification of MuMax3, AIP Adv. **4**, 107133 (2014).

[42] See Supplemental Material Fig. S4 at http://link.aps.org/supplemental/10.1103/PhysRevB.105.174415 for simulated frequency spectra of the triangular structures.

[43] See Supplemental Material Fig. S5 at http://link.aps.org/supplemental/10.1103/PhysRevB.105.174415 for the simulated mode profiles of SQ-2 for the edge mode (E), three first-order local modes (M), and two higher-order modes (HO).

[44] See Supplemental Material Fig. S6 at http://link.aps.org/supplemental/10.1103/PhysRevB.105.174415 for comparison of experimentally observed scanning Kerr images and simulated mode profiles.

[45] See Supplemental Material Fig. S7 at http://link.aps.org/supplemental/10.1103/PhysRevB.105.174415 for simulated mode profiles of SQ-3.

[46] See Supplemental Material Fig. S8 at http://link.aps.org/supplemental/10.1103/PhysRevB.105.174415 for simulated mode profiles for SQ-2 and Sq-3, and the definition of the edges.

[47] J. Zhou *et al.* dataset for "Precessional dynamics of geometrically scaled magnetostatic spin waves in two-dimensional magnonic fractals", doi: 10.5281/zenodo.6513371.

Correction: The name and affiliation of the third author were missing in the original publication and have been inserted.